Electron bifurcation arises from emergent features of multicofactor enzymes

Anna Wójcik-Augustyn, Łukasz Bujnowicz, Artur Osyczka*, Marcin Sarewicz*

Department of Molecular Biophysics, Faculty of Biochemistry, Biophysics and Biotechnology, Jagiellonian University in Kraków, Gronostajowa 7, 30-387 Kraków, Poland

Corresponding authors: email: marcin.sarewicz@uj.edu.pl; email: artur.osyczka@uj.edu.pl

Abstract

Quinone-based electron bifurcation (EB) catalyzed by cytochrome bc_1 ($cytbc_1$) plays a critical role in energy conversion during respiration and photosynthesis. The canonical EB model (CEB), grounded in equilibrium redox potentials, dictates the order of initial EB steps with initial reduction of high-potential iron-sulfur cluster (2Fe2S) by quinol followed by reduction of low-potential heme b_L (b_L) by semiquinone. However, this concept falls short in explaining several experimental observations, including intermediate semiquinone spin-coupled to 2Fe2S and the absence of short-circuiting. We applied quantum mechanical calculations on large cluster models of $cytbc_1$, encompassing both 2Fe2S and b_L, to investigate the early stages of EB. Our results reveal that EB is an emergent property of an integrated system of redox cofactors, where transient charge separations dynamically modulate electron affinities. In this system, electron transfer initiates preferentially toward b_L, indicating a departure from the conventional sequence proposed by CEB. Based on this finding we introduce an EMBER (*EMergent B_L-first Electron Routing*) mechanism of EB and show by electron paramagnetic resonance spectroscopy that predictions derived from this mechanism receive strong experimental validation. We argue that EMBER explains the observed stability of semiquinone coupled to 2Fe2S and suppression of energy wasting short-circuits without additional assumptions. It highlights the importance of dynamic electrostatic interactions in shaping electron transfer pathways in biological systems. In general, the concept of emergence inherent to EMBER offers a mechanistic framework applicable to a broad range of multi-cofactor redox enzymes beyond $cytbc_1$.

Introduction

The quinone-based electronic bifurcation (EB) is a crucial process that maximizes the efficiency of energy conversion during respiration and photosynthesis (*1–5*). Although flavin-based EB has also been identified in some enzymes, the present work focuses on the mechanism of EB catalyzed by cytochromes (cyt) bc of the Rieske/b family, including cyt bc_1 ($cytbc_1$) in bacteria, mitochondrial complex III, and $cytb_6f$ in plants (*2*, *6*, *7*). These enzymes share a similar homodimeric structure across all organisms, exhibiting nearly identical core compositions (Fig. 1A) and spatial arrangements of redox cofactors (Fig. 1B) as well as catalytic sites for quinol (QH_2) oxidation (Q_o) and quinone (Q) reduction (Q_i) (*2*, *8*). In each monomer, the cofactors are branched into two chains — low- and high-potential — with Q_o located between them (Fig. 1C). Upon binding to this site, QH_2 becomes flanked by two cofactors: the iron–sulfur cluster (2Fe2S) from the high-potential chain and heme b_L (b_L) from the low-potential chain.

In $cytbc_1$, EB relies on the two-electron oxidation of QH_2, with each electron diverging into a different direction by transfer to distinct electron acceptors, b_L and 2Fe2S:

$$b_L \leftarrow QH_2 \rightarrow 2Fe2S$$

A one-to-one correlation between the number of electrons transferred from QH_2 to b_L and to 2Fe2S is expected to ensure maximal energy conservation efficiency, while preventing direct electron exchange between b_L and 2Fe2S. Although this process appears conceptually simple, it has never been reproduced in synthetic systems (*9*).

The general framework for EB mechanism, originally proposed by Mitchell, was based on the formalism of equilibrium electrochemistry (*10*, *11*). It describes EB as two consecutive one-electron steps, with the Q/QH_2 redox reaction divided into two half-reactions involving the SQ/QH_2 and Q/SQ redox couples (where SQ and Q denote semiquinone and quinone, respectively). These couples are proposed to differ significantly in their redox midpoint potentials (E_m), with the SQ/QH_2 couple being very high-potential (>400 mV) and the Q/SQ couple being very low-potential (~−200 mV) (*12*, *13*). This suggests that EB is driven by large (more than 600 mV) differences between these couples. Accordingly, EB is assumed to begin with an uphill oxidation of QH_2 to SQ by 2Fe2S (E_m^{2Fe2S} ~300 mV), followed by downhill oxidation of SQ to Q by b_L (E_m^{bL} ~−120 mV). This specific sequence of QH_2 oxidation—first by 2Fe2S and then by b_L—derived from consideration of E_m values for the immediate acceptors (i.e. 2Fe2S and b_L) and the $Q/SQ/QH_2$ triad, has become the widely-accepted EB mechanism and the basis for interpreting both experimental and computational studies. Hereafter, this model is referred to as the canonical EB mechanism (CEB).

Several important consequences follow from CEB. First, SQ is expected to be transient, as the first step is endoergic while the second is exoergic. Consequently, SQ is presumed to be highly

unstable and potentially a substrate for superoxide radical formation due to low E_m of Q/SQ couple (*14*). This inherent instability may explain the long-standing challenges associated with the direct detection of SQ. Second, considering the E_m values of b_L, 2Fe2S, and the Q/SQ/QH_2 triad, the overall reaction should, under certain conditions, be susceptible to short-circuits—that is, quinone-mediated electron transfer from b_L to 2Fe2S (*2*, *4*). This issue becomes especially problematic in understanding the inhibition of $cytbc_1$ by antimycin (*15*, *16*). This inhibitor is thought to promote conditions favoring short-circuiting; however, such events remain experimentally undetectable. On the other hand, under non-equilibrium conditions in the presence of antimycin, relatively large amounts of SQ spin-coupled to $2Fe2S^{red}$ (SQ–$2Fe2S^{red}$) and small amounts of SQ free radical signal have been detected (*17–21*). Yet, the roles of these species in EB remain poorly understood. These unresolved observations have long hindered full mechanistic understanding of EB in $cytbc_1$. Over the years, various models have been proposed, yet the aforementioned issues have never been satisfactorily explained (*2*). Consequently, several, often mutually exclusive, models of EB coexist (*13*, *22–27*), raising the concern that a fundamental principle underlying efficient QH_2 oxidation by $cytbc_1$ might still be missing.

Here, we employed quantum mechanical (QM) calculations to analyze EB in $cytbc_1$ at the level of the electronic wave function (with the main methodological assumptions detailed in the SI), to clarify the roles of SQ and SQ–$2Fe2S^{red}$ in suppressing short circuits for antimycin-inhibited $cytbc_1$ from *Rhodobacter capsulatus*. To this end, we performed density functional theory (DFT) analyses on models containing both b_L and 2Fe2S cofactors as inseparable components of the EB reaction. To the best of our knowledge, this approach has not been previously applied in studies of EB mechanism in $cytbc_1$ and was chosen to avoid—or at least minimize—the artificial selection of reaction sequence inherent in models that isolate individual one-electron reactions. The results demonstrate that all redox-active elements act as an integrated system of cofactors, whose behavior cannot be reproduced by two separate models comprising the quinone molecule and either b_L or 2Fe2S. In particular, we show that the initiation of EB deviates significantly from CEB and proceeds through previously unconsidered states that are, however, consistent with results from electron paramagnetic resonance (EPR) spectroscopy. This resolves the apparent discrepancy between reports detecting semiquinone intermediates within the Q_o site of $cytbc_1$ and $cytb_6f$, lack of short-circuiting and mechanism of antimycin inhibition. If our model correctly describes the EB mechanism, it also underscores the potential limitations of using equilibrium-determined E_m values to construct each step of the reaction. Charge separations, resulting from eTs and pTs within the protein interior, can modify interactions (Coulombic, for example) between cofactors, leading to transient changes in their electron affinities.

We believe that our mechanism offers a unified explanation for several long-standing challenges and may guide designing of synthetic systems in the future.

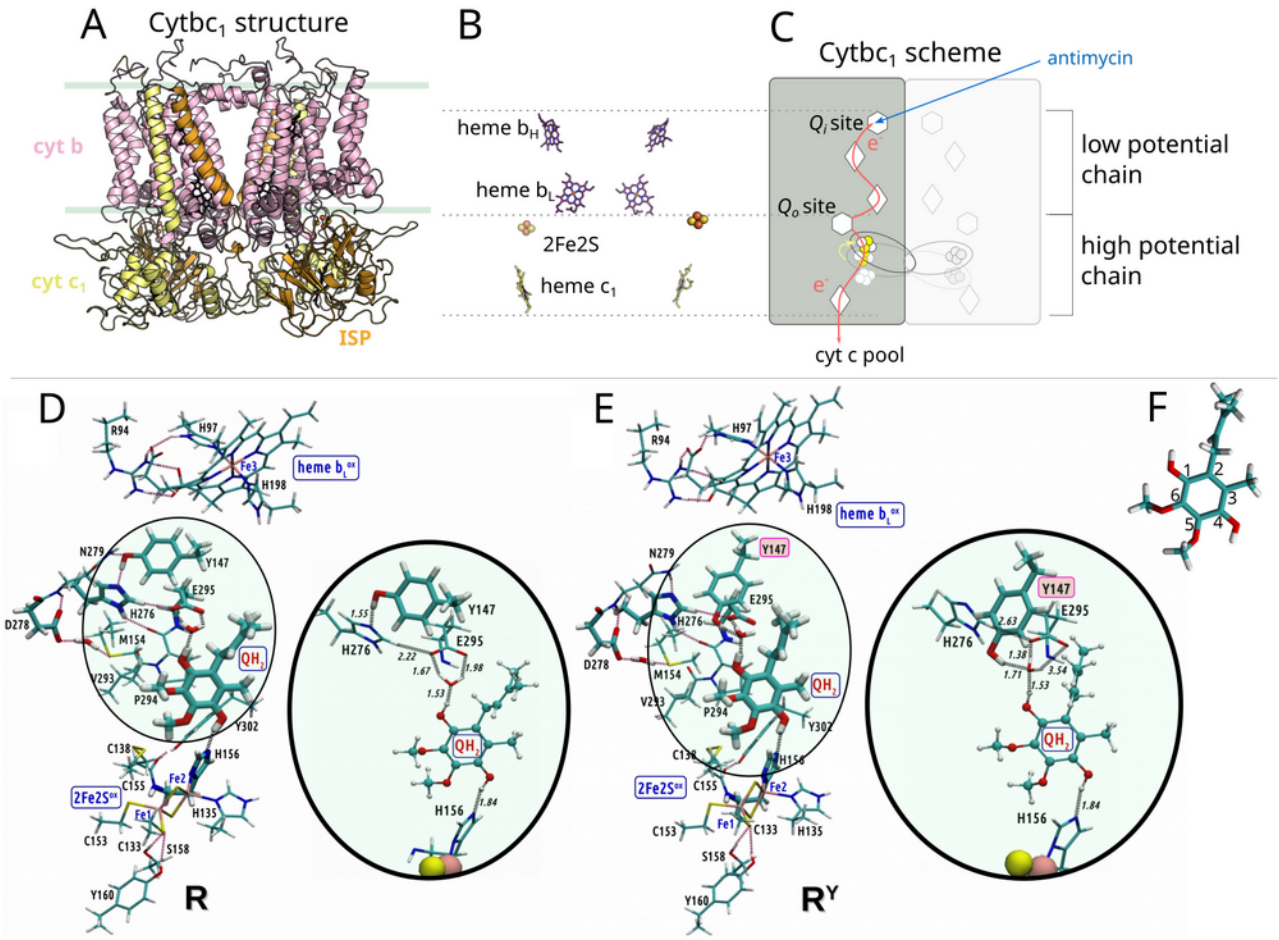

Figure 1. Overview of the structural elements of cytbc$_1$. A) The crystallographic model of the cytbc$_1$ dimer from *Rhodobacter capsulatus* (PDB ID: 1ZRT). Each monomer consists of 3 catalytic subunits: cytochrome b (cyt b), cytochrome (cyt c$_1$) and iron-sulfur protein (ISP). B) The spatial arrangement of redox-active cofactors: hemes b$_L$, b$_H$ of cyt b, 2FeS of ISP, heme c$_1$ of cyt c$_1$. C) General pathways for electrons (*red arrows*) released upon oxidation of QH_2 at Q_o (*white hexagon*). EB directs one electron to high potential chain (consisting of 2Fe2S, c$_1$ and c) and one electron to the low potential chain (consisting of b$_L$, b$_H$ and Q_i). *White diamonds* denote hemes, *circles* denote 2Fe2S. Yellow arrow indicates movement of the head domain of ISP (ISP-HD) containing 2Fe2S between cyt b and cyt c$_1$. The blue arrow shows where inhibitor antimycin binds. For simplicity, the scheme shows eT in one monomer. D) and E) show optimized initial structures of QM model with two possible conformations of cytb:Y147: (D) **R** with Y147 directed toward cytb:H276, and (E) **R^Y** with Y147 directed toward the bound QH_2. Fragments of the models, highlighting the different conformations of the Y147 side chain, are magnified. F) The quinone moiety with the carbon atom numbering of the ring indicated.

Results

To understand how nature realizes EB at a fundamental level, we conducted QM calculations of possible enzyme-catalyzed reactions using models based on cytbc$_1$ crystallographic structures from *Rhodobacter capsulatus*. Our basic assumptions require defining what we consider

as the EB reaction. In this work, EB is viewed as a minimal cascade of reactions leading to a stable, low-energy state containing the product Q — which corresponds to a state that can be detected experimentally as the dominant state under equilibrium conditions, i.e., upon depletion of reaction substrates. In this respect, we consider only the primary EB steps, rather than the entire catalytic Q cycle. The models covered either Q_o or Q_i. For the first time, and unlike as in previous studies (*28–31*), the QM model of Q_o included both acceptors of electrons from QH_2: 2Fe2S and b_L (Fig. 1D, E). In the starting state, QH_2 forms a hydrogen bond to deprotonated H156 of iron-sulfur protein (*R. capsulatus* numbering) and *via* water molecule to negatively charged E295 of cytb, at the time when immediate electron acceptors 2Fe2S and b_L are oxidized. Y147 of cytb adopts two conformations: away from or close to E295 (**R** in Fig. 1D or $\mathbf{R^Y}$ in Fig. 1E, respectively and Fig. S1). The rationale behind selection of the starting state is explained in SI.

Inability to reproduce inital reaction steps in accordance to CEB. Initially, following the assumptions of CEB, we tested the scenario in which the reaction is expected to start from **R** or $\mathbf{R^Y}$ with protonation of H156 by C4-OH of QH_2 (atom numbering in Fig. 1F), followed by eT to 2Fe2S. Neither of expected structures containing b_L^{ox}, QH^-, protonated H156 and oxidized 2Fe2S ($2Fe2S^{ox}$), nor those with b_L^{ox}, SQH/SQ^- and reduced 2Fe2S ($2Fe2S^{red}$) could be obtained by QM, even after providing initial electronic configuration of these expected states (details in SI). Instead, relocation of proton from C4-OH to H156 is accompanied by both: pT from C1-OH to E295 and simultaneous eT from QH_2 to b_L. This led to the intermediate containing SQ^-, b_L^{red}, and $2Fe2S^{ox}$ (**I2** in Fig. 2A and **I2** or $\mathbf{I2^Y}$ in Fig. S2), which appeared in a clear contradiction with predictions based on CEB. Such the state seems quite advanced in the progression of EB as it must have resulted from at least two pTs and one eT (protons are already on H156 and E295 and electron is on b_L). It thus appears that transition from **R**/$\mathbf{R^Y}$ to **I2**/$\mathbf{I2^Y}$ might involve an intermediate step to be considered. Therefore, we went back to the beginning of the reaction and tested how **R** or $\mathbf{R^Y}$ responses to the initial water-mediated pT from C1-OH to E295. Surprisingly, this pT was coupled to eT from QH_2 to b_L, leading to **I1** or $\mathbf{I1^Y}$, (states containing SQH, b_L^{red} and $2Fe2S^{ox}$, Fig. 2A and Fig. S2). The emergence of b_L^{red} next to $2Fe2S^{ox}$ was unexpected result, given that E_ms of b_L and 2Fe2S , determined for proteins under equilibrium, suggests a higher electron affinity for 2Fe2S than b_L. This prompted us to scrutinize the electronic structure of **R**, which was taken as the most probable state of the Q_o-QH_2 complex ($\mathbf{R^Y}$ and following $\mathbf{I1^Y}$ were 1 and 5 kcal/mol less stable than **R** and **I1**, respectively).

Asymmetry in charge and spin distribution in the initial structure. In **R**, there is a shift of electron density from QH_2 toward b_L, associated with a spread of unpaired α spin density (SD) over M154 and D278 of cytb toward QH_2 (Fig. S3). At the same time, α (S_{Fe1}=5/2) and β (S_{Fe2} = -5/2) SD are present on iron ions of $2Fe2S^{ox}$ but antiferromagnetism cancels the net spin. Such the

electronic structure indicates that the highest occupied and the lowest unoccupied molecular orbital (HOMO and LUMO, respectively) are located on QH_2 and b_L, respectively (Fig. S4). Shifting of electron density toward b_L imposes a heterogeneous distribution of the local electric potential around the quinone ring with the more negative potential at the region of C1-OH compared to C4-OH (Fig. S3B, red arrow). This polarization along with the location of HOMO and LUMO determines eT from C1-OH to b_L accompanied with pT to carboxyl group of E295, resulting in state **I1** (Fig. 2A and S2A). It is important to emphasize that it was not possible to obtain **I1** in models deprived of the cluster (Fig. S5-S8). Furthermore, for the model deprived b_L, we obtained stable state containing SQ-2Fe2S^{red} (Fig. S9) similarly to previous work (*28–31*). If such the models were to truly reproduce the first EB step, one would expect detection of EPR signal of SQ-2Fe2S^{red} for cytbc$_1$ with b_L knocked-out, which is not the case (*32*). Such approach for determining initial steps of EB suffers from the *a priori* setting the sequence of the reactions. Clearly, reaching of **I1** requires the presence of both b_L and 2Fe2S, despite apparent lack of involvement of the latter in this process. Additionally, the models of **R** variants with either protonated H156 and 2Fe2S^{ox} or deprotonated H156 without the cluster also failed to show any signs of progress to **I1** (Fig. S10).

Reversible EB stages on a way toward product. The state **I1** passes to **I2** by shifting H^+ originating from the C4-OH group of SQH toward H156. The RMSD parameter comparing the positions of all atoms in **R, I1** and **I2** is about 0.06Å indicating no structural rearrangement upon **R↔I1↔I2** transitions (Fig. 2B).

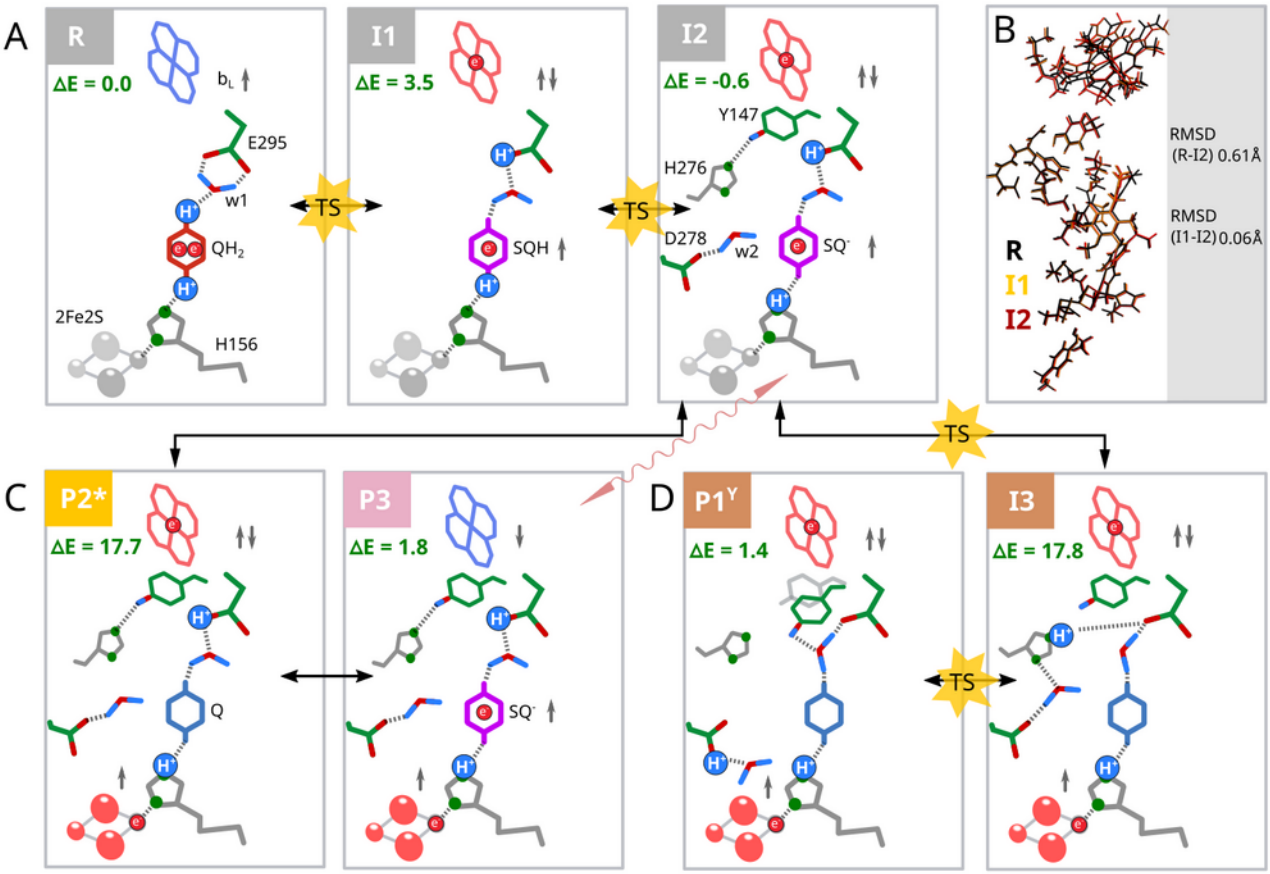

Figure 2. Primary steps of EB without involvement of eT from b_L to b_H. A) **R** denotes a starting state comprising b_L^{ox} (*blue crossed-hexagon*), QH_2 (*black hexagon*), and $2Fe2S^{ox}$ (*grey ovals*). The reaction progresses through transition states (TS *yellow stars* representing the energy barriers) to **I1** and **I2**, containing b_L^{red} (*red crossed-hexagon*) and SQH, or SQ^- (*magenta hexagon*), respectively. B) Superimposed geometries of **R**, **I1**, and **I2**. C) Evolution of **I2** to stable **P3** containing b_L^{ox}, SQ^-, and $2Fe2S^{red}$ (*red ovals*), via unstable **P2*** with b_L^{red}, Q (*blue hexagon*), and $2Fe2S^{red}$. Electron tunneling directly connecting **I2** and **P3** is shown as wavy arrow. D) Evolution of **I2** to $\mathbf{P1^Y}$ containing b_L^{red}, Q, and $2Fe2S^{red}$ *via* high energy **I3** and two transition states. Gray arrows indicate the net spin corresponding to the redox state of the substrate and cofactors. Amino acid side chains are shown when their protonation and/or conformation state is significant. Important water molecules are labeled as "w1" and "w2" and protons derived from QH_2 in the given state are represented by blue circles.

The energy levels of **R**, **I1** and **I2** are relatively close to each other, which means that at room temperature (~300 K) they are expected to be similarly populated, albeit not equally, and they should transform from one to another. Thus, **R**, **I1** and **I2** are considered as degenerate, coexisting states. At this stage, the hydrogen bonds involving protonated E295 and protonated H156 stabilize **R↔I1↔I2** triad (Fig. 2A) and it is impossible to obtain low energy system containing product (Q, $2Fe2S^{red}$ and b_L^{red}).

We first searched for states containing stable product under conditions when electron on b_L cannot advance to b_H (like in antimycin-inhibited enzyme). One tested reaction involved elongation of the H-bond between SQ^- and protonated H156. This resulted in unstable **P2*** (Fig. 2C and Fig. S11) which immediately relaxed back to **I2** or evolved to **P3** (b_L^{ox} along with SQ ferromagnetically-

coupled to 2Fe2S^{red}, (discussion in SI, Fig. S12). Thus, **P2*** should be considered as a transition state (its estimated energy is +18 kcal/mol) between **I2** and **P3**. We note that nearly identical geometry of nuclei in **I2** and **P3** indicates possibility for electron tunneling, which connects these states. The second tested reaction involved shifting the proton away from E295 to D278. This resulted in relatively stable **P1^{Y}** containing Q (Fig. 2D). However, as reaching of this state from **I2** is slightly endoergic and required crossing two barriers with a high energy state in between (**I3**, +18 kcal/mol, Fig S13), this process is unlikely. Consequently, the enzyme gets stuck in the states **R↔I1↔I2** and **P3.**

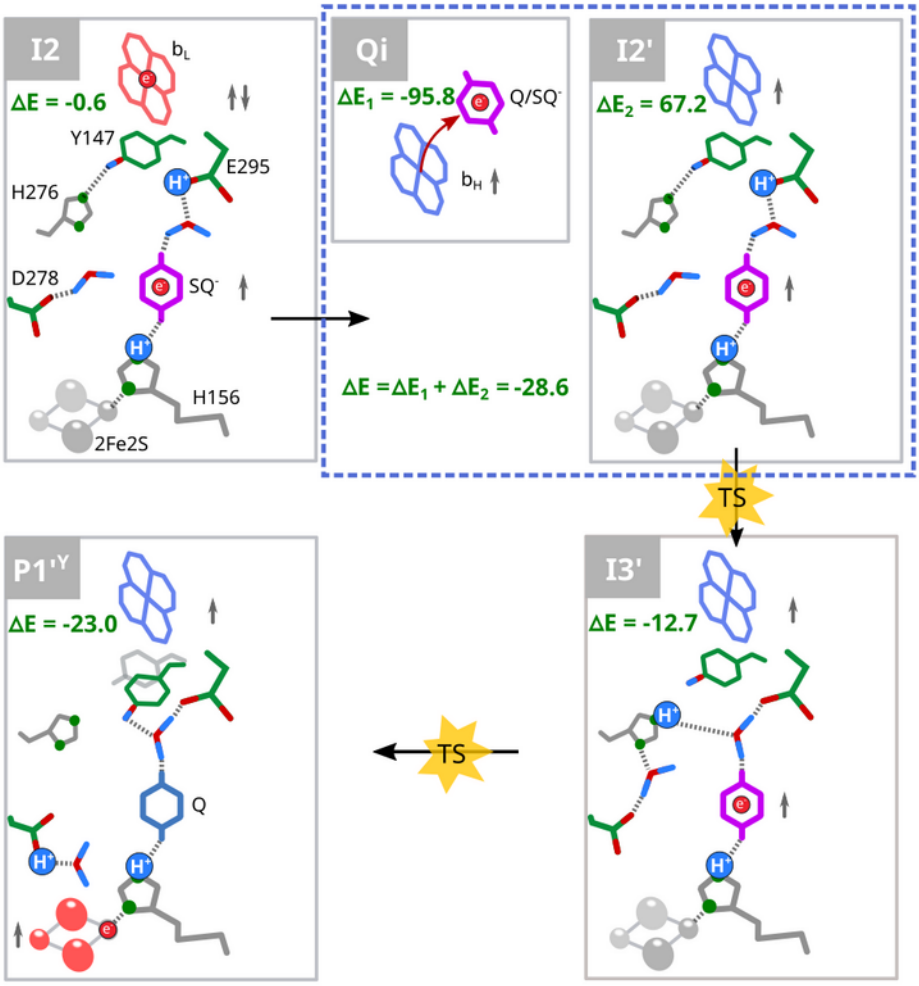

Figure 3. Completion of EB involving energy released during eT from b_H to Q_i. The eT from b_L to b_H and subsequently to Q_i provides a highly exoergic step that resolves the **R↔I1↔I2** degeneration (see Fig. 2), driving the reaction from **I2** toward **I3'**. The energy associated with this reaction was calculated using the states **Qi** and **I2'** considered together (*blue dashed square*). **P1'^{Y}** denotes the final state of EB containing Q, 2Fe2S^{red} and protonated D278. The symbols are consistent with those used in Fig. 2. Red arrow indicates eT.

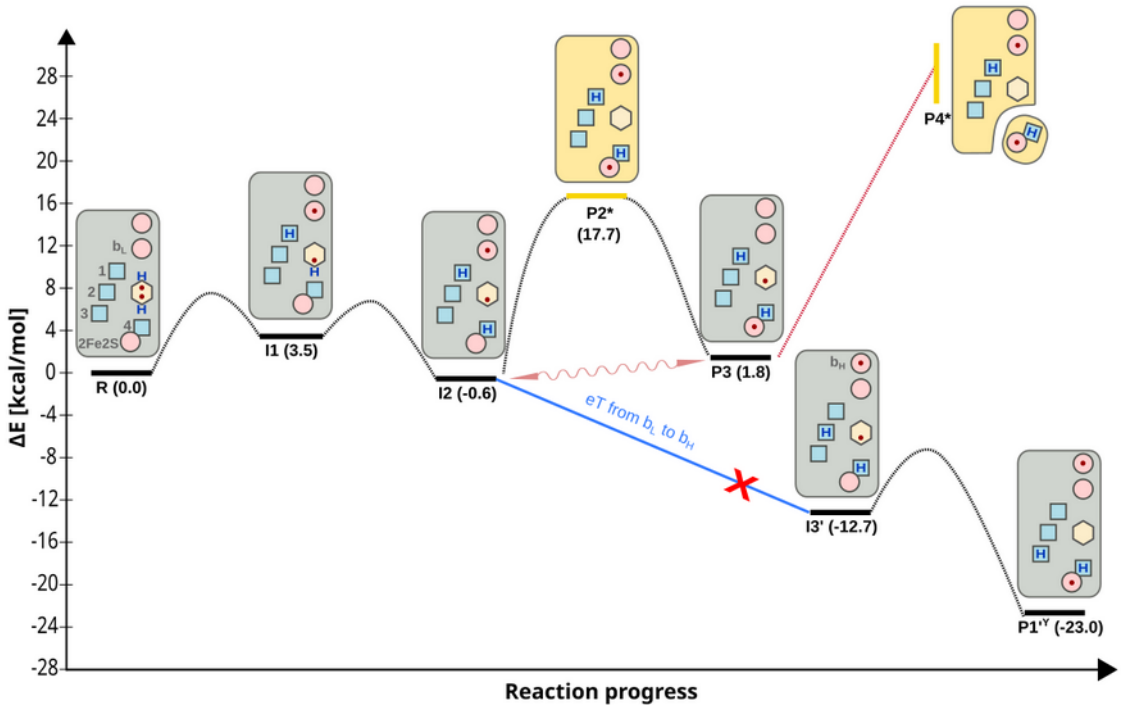

Figure 4. The EMBER mechanism of EB. Solid black lines represent relative energy levels (numbers in parentheses) of the states on the way from the substrate (**R**) to product (**P1'^{Y}**). Yellow solid line represents energy level of transition state (**P2***). Red circles – electron acceptors; blue squares – proton acceptors 1, 2, 3 in cyt b (in *R. capsulatus* E295, H276, D278, respectively), and 4 in ISP (histidine ligand to 2Fe2S); yellow hexagon – quinone moiety; red dots and blue "H" – electrons and protons derived from QH_2; red cross - inhibition by antimycin; wavy arrow – electron tunneling; dotted lines illustrate barriers between states. Red dotted line denotes the possibility of quinone formation **P4*** from **P3** by elongation of the distance between ISP and the Qo. The energy level of **P4*** increases due to uncompensated breaking interactions, thus cannot be deterimned precisely (yellow vertical line).

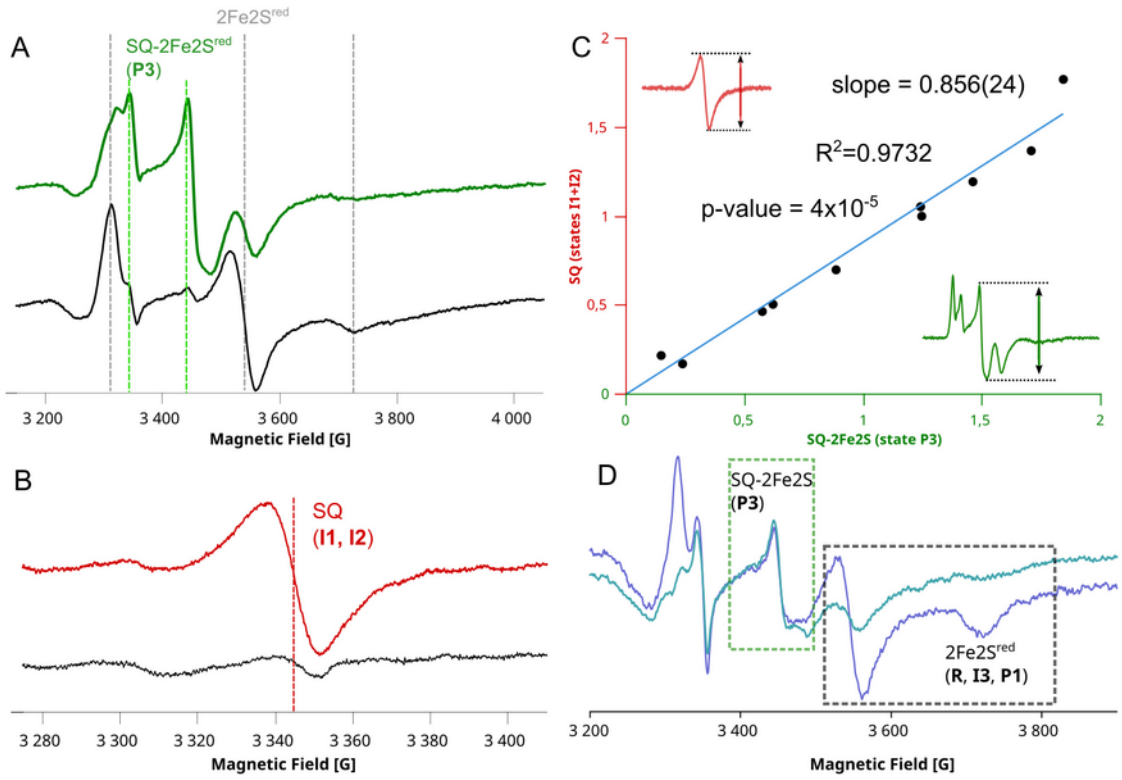

Figure 5. Experimental validation of predictions derived from the EMBER mechanism of the electron bifurcation (EB) mechanism using antimycin-inhibited cytbc$_1$. (A) EPR spectra of 2Fe2S^{red} and SQ–2Fe2S^{red} (P3) recorded under equilibrium (black) and non-equilibrium (green; 1 s after substrate addition) conditions. Dashed vertical lines indicate the main EPR transitions of 2Fe2S^{red} (gray) and SQ–2Fe2S^{red} (green). **(B)** SQ radical signal (I1 or I2) detected in the same samples as in A, under equilibrium (black) and non-equilibrium (red) conditions. **(C)** Expected linear correlation between the populations of enzyme molecules in **I1**/**I2** and **P3**. **(D)** Double-mixing EPR experiment showing spectra of enzyme pre-set to the **P3** state, followed by mixing with buffer (blue) and with an additional portion of oxidized cytc (turquoise). Black and green boxes highlight regions corresponding to 2Fe2S^{red} and SQ–2Fe2S^{red}, respectively.

Releases from degenerate states and emergence of product. In further search for exoergic processes that would push EB toward low-energy product, we estimated the net energetic cost associated with eT from b_L through b_H to Q_i (Fig. 3). We considered a state **I2'** which is a result of removal of electron from b_L in **I2**, and various states of the complementary model that mimicked the acceptance of this electron. The complementary models encompassed b_H and quinone at Q_i (details in SI and Fig. S14). The results indicate that the transition from **I2** to **I2'** would be endoergic (+67,2 kcal/mol) if the complementary model was not included. However, the average energy released per electron delivered to Q_i (-95.8 kcal/mol) lowers energy of **I2'** to -28,6 kcal/mol (Fig. 3). In this way, eT from Q_o to Q_i makes EB exoergic allowing Q_o to departure from degenerated states **R↔I1↔I2** and **P3** (the latter state is unlikely to be formed when this eT is not blocked). The net energy released in Q_i drives the enzyme to overcome local barrier associated with pT from E295 to H276 (state **I3'**). The following pT from H276 to D278 is coupled to eT from SQ

to 2Fe2S which weakens the interaction between quinone moiety and protonated H156 (the H-bond elongates from 1.5 to 2.0 Å, Fig. S15, S16). This reaction is the final step of EB leading to the low-energy state **P1'^{Y}** (-23.0 kcal/mol in respect to **R**) containing product (quinone).

We note that while the essence in the departure for degenerated states lies in effective removal of the proton away from the quinone ring, the exact pT path is not a determinant of this process but influences its efficiency. The process might be tolerant to mutational changes and the residues that build the path may vary in different species (*33–36*). We also note that, in this mechanism, completion of EB does not require the motion of the ISP away from Q_o. It is worth mentioning about recent reports on structures of cytbc$_1$ for which ISP does not move during the catalytic cycle (*37*). When the motion occurs during further steps of enzymatic catalysis that follow **P1'^{Y}**, transferring electron toward more remote cofactors (c-type hemes) it further lowers the energy of the system. However, as mentioned above, these steps remain beyond consideration of this work.

Figure 4 summarizes the most probable enzyme states that constitute the pathway of EB-based quinol oxidation identified by QM (see Fig. S17 for all considered states). When QH_2 bound in Q_o encounters 2Fe2S^{ox} and b_L^{ox} (**R**), the negative charge from the quinol moiety initially shifts toward b_L (**I1**, **I2**). ET from the resulting SQ to 2Fe2S (**I3′**, **P1$^{'Y}$**) is powered by the energy released upon electron transfer from b_L to Q_i (blue line). Without this energetic input, the enzyme is trapped in states **R**, **I1**, **I2**, and P3, with no possibility of reaching a low-energy product state.

It should be emphasized that our QM models included both immediate electron acceptors (2Fe2S and b_L) and proton acceptors at every step of the reaction. In doing so, we avoided predefining the sequence of events characteristic of canonical EB modeling, where the reaction is split into two sequential one-electron transfers: first from QH_2 to 2Fe2S, then from semiquinone to b_L. This sequential view contrasts with the mechanism inferred from our simulations, where electron flow begins with b_L and proceeds *via* an energetically favorable cooperative route.

To distinguish this mechanistic insight, we introduce the term EMBER (*EMergent B_L-first Electron Routing*) which refers to a concept highlighting the spontaneous and energetically driven appearance of the alternative EB pathway not anticipated by conventional CEB assumptions. This mechanism, free from imposed constraints, reveals a bifurcation behavior fundamentally distinct from previously proposed models.

The initial shift of negative charge toward b_L does not occur in the models of **R** deprived of 2Fe2S (Fig. S5-S8). This removes possibility of reproducing the sequence of reactions underlying EMBER and identified through the *ab initio EB* model by splitting this model into two separate one-electron reactions. We also checked if the sequence of reactions predicted by the models based on CEB can be reproduced by analogous splitting of the model into two reactions. For this case, we

tested the possibility of the first eT from QH_2 to 2Fe2S in model of **R** deprived of b_L. We found that SQ along with $2Fe2S^{red}$ were formed but, contrary to the assumptions of CEB and consistent with recent proposal (*28*), the process occurred to be exoergic. The complementary reaction of the second eT from SQ to b_L (reproduced in **P3** deprived of 2Fe2S) is endoergic. This introduces a high energy barrier that cannot be crossed. As electron does not reach b_L, further eT toward Q_i is not possible. The system is expected to get stuck in the state with very stable SQ, which is contradictory to CEB assumptions and experimental observations. Clearly, splitting of EB into two separate eT reactions seems leading to the artifacts of either a lack of the initial reaction or a formation of the overly stable SQ. Thus, the occurrence of EB must be an inherent feature of the emergent system including immediate electron and proton donors and acceptors.

Confronting the EMBER mechanism with experiment. According to EMBER mechanism, antimycin-inhibited $cytbc_1$ exposed to substrates gets trapped in states **R↔I1↔I2↔P3** (Fig 4). **P3** contains SQ^- ferromagnetically coupled to $2Fe2S^{red}$ featuring rhombic spectrum, with the most prominent transition at g=1.94, clearly distingushable from $2Fe2S^{red}$ g=1.90 (Fig. 5A, green and black, respectively). **I1** and **I2** contain paramagnetic SQ^- species of expected typical radical g=2.0 transition in EPR spectrum which disappears after reaching the equilibrium (Fig. 5B, red and black, respectively). Given that **I1**/**I2** and **P3** are energetically close to each other, the populations of **I1**/**I2** and **P3** should be linearly correlated and proportional to the number of molecules that initiate EB. This is clearly seen in the analysis of the correlation (p-value < 0.001) between amplitudes of these two signals obtained from the experiment (Fig 5C). Additionally, since **P3** contains b_L^{ox}, the signal at g=1.94 should be accompanied by that of b_L^{ox} and this result systematically repeats in various experiments (*17*, *18*). The model also predicts that the formation and decay of **P3** is slow as it requires crossing **P2*** that lies ~18 kcal/mol above both **I2** and **P3**. However, since a tunneling process also contribute to transitions between **I2** and **P3** states, they may equilibrate even in frozen enzyme thus it is technically not feasible to trace the transition between **I2** and **P3** by freeze-quench EPR. On the other hand, when antimycin is not present and b_H can accept electron from b_L, **I1** and **I2** are transient while **P3** is kinetically isolated thus not formed at all (*38*). Thus, paramagnetic identities of **I1**, **I2** and **P3** should be rather undetectable by EPR under equilibrium or in non-inhibited enzyme. This explains long-standing difficulty in trapping SQ at Q_o in the non-inhibited enzyme. According to the model, **P3** formation requires electron exchange involving b_L. Indeed, spectroscopic feature of **P3** was not detected in the mutant in which such exchange has been disabled by changing the b_L axial ligand (*32*). Kinetic isolation of **P3** seems exclude the possibility that SQ-$2Fe2S^{red}$ is the first step of EB but supports order of reaction summarized in Fig. 4. According to the diagram, the dissociation of 2Fe2S from the Q_o site occupied by SQ requires overcoming significant energy barriers (**P2***, **P4***). In particular, the decay of **P3** via the high-

energy **P4*** intermediate—posing a risk of short-circuiting the enzyme upon 2Fe2S oxidation—is considered highly improbable.

This prediction is strongly supported by the experiment shown in Fig. 5D. When the antimycin-inhibited enzyme is premixed with substrates (QH_2 and cyt c), we detect populations containing **P3** and all other possible states with $2Fe2S^{red}$ (Fig. 5D, blue spectrum). Subsequent rapid mixing and freezing with only cyt c leads to significant oxidation of $2Fe2S^{red}$ in molecules where the ISP can move freely. However, the signal reflecting **P3** remains nearly unchanged, suggesting that **P3** cannot rapidly exchange electrons with cyt c molecules, thus **P3** locks the domain at the Q_o site in a manner similar to stigmatellin.

Discussion

In this study, we performed a series of QM calculations on various possible states of the $cytbc_1$ to investigate the mechanism of the initial stages of EB. Our motivation stemmed from certain interpretative challenges related to the observed enzyme states, particularly under conditions where the enzyme is inhibited by antimycin (*2*). According to CEB, which assumes that equilibrium redox potentials can be applied at each reaction step, and which considers a large potential separation between the Q/SQ and SQ/QH_2 pairs, the enzyme would be expected to be prone to short-circuiting (*4*, *16*). Such behavior should be especially prominent when the Q_i site is blocked by antimycin, when the quinone pool in the membrane is highly reduced, or under a substantial transmembrane electrical gradient. However, experimental observations do not support the occurrence of such short-circuiting. Moreover, the classical model predicts an extremely low occupancy of the Q_o site by semiquinone, aiming to minimize potential side reactions such as short-circuits or radical formation (*14*, *19*, *21*, *39*). Nevertheless, this prediction is not fully consistent with experimental findings on the antimycin-inhibited bacterial $cytbc_1$, which reveal a relatively high concentration of SQ-$2Fe2S^{red}$ (**P3** state), despite the absence of detectable short-circuiting (*17*, *18*, *40*, *41*).

In our work we attempted to model the EB reactions by retain as many reaction-relevant elements as possible in order to reproduce EB in $cytbc_1$. Consequently, large QM cluster models were employed, which precluded calculations of transition states and thus prevented estimation of reaction rates. The approach to use the large models was further supported by our observation that QM optimization leads to different electronic states when the models are artificially divided into parts that consider only a single cofactor at a time, which in turn may impose an artificial reaction sequence by predefining the order of events in such fragmented models. Although we could not calculate the reaction rates, we propose that, given the small structural rearrangements observed during optimization, it is reasonable to assume that large energy barriers are unlikely. The only barrier estimated corresponded to **P2***, which likely accounts for the experimentally observed

kinetic isolation of the state containing SQ-2Fe2S^{red} under conditions of blocked eT from b_L to b_H. Therefore, it appears unlikely that **P3** serves as the starting point for electron bifurcation under conditions where b_H is oxidized and poised to accept electrons from b_L. In this case, we propose that **I1** and **I2** are the primary reactions of QH_2 oxidation by cytbc$_1$, since the states **R** or **R^Y** converges to **I1**. On the other hand, the arrest of the ISP domain in the **P3** state prevents it from leaving the Q_o site, and thus limits the possibility of radical generation. Additionally, the immobilized ISP prevents oxidation of 2Fe2S^{red} which blocks electron transfer from SQ to the returning 2Fe2S^{ox}. Although the reason why the ISP does not move in the **P3** state is not known, it seems an experimentally confirmed fact (Fig. 5D).

According to our mechanism, the reaction is initiated by electron transfer to b_L, which represents the most controversial finding of this study. This observation is inconsistent with CEB (*10*, *11*, *13*). Interpreting this behavior within the framework of classical electrochemical theory suggests that equilibrium redox potentials cannot be strictly applied to each step of the reaction but instead describe the final thermodynamic relationships between the reduced and oxidized populations of all redox elements once the system has reached equilibrium when reaction is complete. We emphasize that we do not challenge the general validity of Marcus theory (*42*). Rather, we propose that under certain transient conditions present in cytbc$_1$ (and possibly in other multicofactor enzymes), additional dynamic factors (like charge separations due to eT and pT) may modulate electron affinity around particular redox cofactors. This may be attributed to dynamic changes in the protonation states of amino acid residues and in the redox states of cofactors during the course of the reaction. Previous studies have shown that the reduction of one heme can lower the redox potential of an adjacent heme through Coulombic interactions (*43*). Such changes in electrostatic interactions often lead to splits or stretching the Nernst curves (due to a lowering of the n parameter below 1) measured for cofactors spatially bonded by the protein structure (*44*). The effect of such interactions has been demonstrated for electron distribution in dimeric cytb$_6$f (*45*). In the case of hemes b at distances similar to those in cytbc$_1$, shifts of up to ±100 mV should be expected (*26*, *43*). On the other hand, protonation of H156 near 2Fe2S can shift the cluster potential from approximately -120 mV to +300 mV (see fig. 3 in (*46*)). Considering that the measured redox potential values for b_L correspond to conditions where b_H is already reduced, and for 2Fe2S where protonation has already occurred, these values do not reflect the state of the activated enzyme–substrate complex, in which electron bifurcation begins. At the onset of EB, the electron affinities of b_L and 2Fe2S may be relatively similar from the 'QH_2 point of view,' because at this stage heme b_H is oxidized and H156 at the 2Fe2S cluster is deprotonated. Consequently, large potential separations between Q/SQ and SQ/QH_2 are not required at the early stages of the reaction. By contrast, after bifurcation is completed and equilibrium is established, the system adopts a state in which b_L and

2Fe2S exhibit potentials of approximately -120 mV and +300 mV, respectively, as determined from equilibrium redox titrations (*47*).

The EMBER mechanism presented here considers the electron bifurcation mechanism catalyzed by $cytbc_1$ at a fundamental level, providing a comprehensive explanatory framework for both current and future experiments. We believe that using this mechanism and abandoning the canonical electron bifurcation concept, several observations that were previously difficult to interpret become clearer, and those that seemed contradictory to one another can now be unified. As the proposed concept of transient changes in electron affinities may apply not only to $cytbc_1$ but also to other multicofactor enzymes, future experiments should aim to confirm or falsify this model.

Materials and Methods

The cluster models for the Q_o and Q_i active sites of $cytbc_1$ were constructed based on crystallographic structures from *Rhodobacter capsulatus* (PDB code: 1ZRT) and *Bos taurus* (PDB code: 1NTZ). The models included key residues, ubiquinol, water molecules, and 2Fe2S, with protonation states assigned using Propka 3.1. QM calculations were performed using Gaussian 16 (*48*), with geometry optimizations carried out at the DFT/B3LYP level of theory including Grimme's D3 dispersion correction with Becke-Johnson damping (*49*, *50*). Final energy was corrected to approximate the protein environment (details in *SI*). Experimental procedures involved freeze-quench and double-mixing experiments to capture intermediate states of $cytbc_1$. Freeze-quench samples were prepared using a Biologic SFM-300 stopped-flow mixer and EPR techniques, with different reaction time points achieved by modulating incubation periods. Double-mixing experiments were conducted using a custom-built multichannel pulse high-current driver, and the oxidation of cytochrome c_1 was monitored spectrophotometrically. EPR measurements were carried out with a Bruker Elexsys E580 spectrometer, using X-band continuous wave spectra at temperatures ranging from 20 K to 200 K. The spectra were normalized using Fe^{3+} citrate as an internal standard. For further details on the modeling, sample preparation, experimental protocols, and EPR measurement conditions, please refer to *SI*.

Reference and Notes

1. W. Nitschke, M. J. Russell, Redox bifurcations: Mechanisms and importance to life now, and at its origin: A widespread means of energy conversion in biology unfolds…. *BioEssays* **34**, 106–109 (2012).

2. M. Sarewicz, S. Pintscher, R. Pietras, A. Borek, Ł. Bujnowicz, G. Hanke, W. A. Cramer, G. Finazzi, A. Osyczka, Catalytic Reactions and Energy Conservation in the Cytochrome bc1 and

b6f Complexes of Energy-Transducing Membranes. *Chemical Reviews* **121**, 2020–2108 (2021).

3. S. Al-Attar, S. de Vries, Energy transduction by respiratory metallo-enzymes: From molecular mechanism to cell physiology. *Coordination Chemistry Reviews* **257**, 64–80 (2013).

4. A. Osyczka, C. C. Moser, F. Daldal, P. L. Dutton, Reversible redox energy coupling in electron transfer chains. *Nature* **427**, 607–612 (2004).

5. J. L. Yuly, P. Zhang, C. E. Lubner, J. W. Peters, D. N. Beratan, Universal free-energy landscape produces efficient and reversible electron bifurcation. *Proc. Natl. Acad. Sci. U.S.A.* **117**, 21045–21051 (2020).

6. A. R. Crofts, The cytochrome bc1 complex: function in the context of structure. *Annual Review of Physiology* **66**, 689–733 (2004).

7. L. A. Malone, M. S. Proctor, A. Hitchcock, C. N. Hunter, M. P. Johnson, Cytochrome b6f – Orchestrator of photosynthetic electron transfer. *Biochimica et Biophysica Acta - Bioenergetics* **1862**, 148380–148380 (2021).

8. E. Darrouzet, J. W. Cooley, F. Daldal, The cytochrome bc1 complex and its homologue the b6f complex: similarities and differences. *Photosynthesis Research* **79**, 25–44 (2004).

9. J. L. Yuly, C. E. Lubner, P. Zhang, D. N. Beratan, J. W. Peters, Electron bifurcation: progress and grand challenges. *Chem. Commun.* **55**, 11823–11832 (2019).

10. P. Mitchell, The protonmotive Q cycle: A general formulation. *FEBS Letters* **59**, 137–139 (1975).

11. A. R. Crofts, S. W. Meinhardt, K. R. Jones, M. Snozzi, The role of the quinone pool in the cyclic electron-transfer chain of Rhodopseudomonas sphaeroides: a modified Q-cycle mechanism. *Biochimica et Biophysica Acta* **723**, 202–218 (1983).

12. L. Bergdoll, F. Ten Brink, W. Nitschke, D. Picot, F. Baymann, From low- to high-potential bioenergetic chains: Thermodynamic constraints of Q-cycle function. *Biochimica et Biophysica Acta - Bioenergetics* **1857**, 1569–1579 (2016).

13. A. Osyczka, C. C. Moser, P. L. Dutton, Fixing the Q cycle. *Trends in Biochemical Sciences* **30**, 176–182 (2005).

14. J. L. Cape, M. K. Bowman, D. M. Kramer, Understanding the cytochrome bc complexes by what they don't do. The Q-cycle at 30. *Trends in Plant Science* **11**, 46–55 (2006).

15. S. Ransac, N. Parisey, J.-P. Mazat, The loneliness of the electrons in the bc1 complex. *Biochimica et Biophysica Acta* **1777**, 1053–1059 (2008).

16. S. Ransac, J.-P. Mazat, How does antimycin inhibit the bc1 complex? A part-time twin. *Biochimica et Biophysica Acta - Bioenergetics* **1797**, 1849–1857 (2010).

17. M. Sarewicz, M. Dutka, S. Pintscher, A. Osyczka, Triplet state of the semiquinone-Rieske cluster as an intermediate of electronic bifurcation catalyzed by cytochrome bc1. *Biochemistry* **52**, 6388–6395 (2013).

18. M. Sarewicz, Ł. Bujnowicz, S. Bhaduri, S. K. Singh, W. A. Cramer, A. Osyczka, Metastable radical state, nonreactive with oxygen, is inherent to catalysis by respiratory and

photosynthetic cytochromes bc1/b6f. *Proceedings of the National Academy of Sciences* **114**, 1323–1328 (2017).

19. J. L. Cape, M. K. Bowman, D. M. Kramer, A semiquinone intermediate generated at the Qo site of the cytochrome bc1 complex: Importance for the Q-cycle and superoxide production. *Proceedings of the National Academy of Sciences of the United States of America* **104**, 7887–7892 (2007).

20. H. Zhang, A. Osyczka, P. L. Dutton, C. C. Moser, Exposing the complex III Qo semiquinone radical. *Biochimica et Biophysica Acta* **1767**, 883–887 (2007).

21. D. Victoria, R. Burton, A. R. Crofts, Role of the -PEWY-glutamate in catalysis at the Qo-site of the Cyt bc1 complex. *Biochimica et Biophysica Acta (BBA) - Bioenergetics* **1827**, 365–386 (2013).

22. U. Brandt, G. von Jagow, Analysis of inhibitor binding to the mitochondrial cytochrome c reductase by fluorescence quench titration. Evidence for a “catalytic switch” at the Qo center. *European Journal of Biochemistry* **195**, 163–170 (1991).

23. L. Esser, X. Gong, S. Yang, L. Yu, C.-A. Yu, D. Xia, Surface-modulated motion switch: Capture and release of iron–sulfur protein in the cytochrome bc1 complex. *Proceedings of the National Academy of Sciences of the United States of America* **103**, 13045–13050 (2006).

24. T. A. Link, The role of the “Rieske” iron sulfur protein in the hydroquinone oxidation (QP) site of the cytochrome bc1 complex. *FEBS letters* **412**, 257–264 (1997).

25. P. R. Rich, The quinone chemistry of bc complexes. *Biochimica et Biophysica Acta* **1658**, 165–171 (2004).

26. R. Springett, The proton pumping mechanism of the bc complex. *Biochimica et Biophysica Acta (BBA) - Bioenergetics* **1862**, 148352 (2021).

27. C. H. Snyder, E. B. Gutierrez-Cirlos, B. L. Trumpower, Evidence for a concerted mechanism of ubiquinol oxidation by the cytochrome bc1 complex. *Journal of Biological Chemistry* **275**, 13535–13541 (2000).

28. M. J. Frisch, G. W. Trucks, H. B. Schlegel, G. E. Scuseria, M. A. Robb, J. R. Cheeseman, G. Scalmani, V. Barone, G. A. Petersson, H. Nakatsuji, X. Li, M. Caricato, A. V. Marenich, J. Bloino, B. G. Janesko, R. Gomperts, B. Mennucci, H. P. Hratchian, J. V. Ortiz, A. F. Izmaylov, J. L. Sonnenberg, Williams, F. Ding, F. Lipparini, F. Egidi, J. Goings, B. Peng, A. Petrone, T. Henderson, D. Ranasinghe, V. G. Zakrzewski, J. Gao, N. Rega, G. Zheng, W. Liang, M. Hada, M. Ehara, K. Toyota, R. Fukuda, J. Hasegawa, M. Ishida, T. Nakajima, Y. Honda, O. Kitao, H. Nakai, T. Vreven, K. Throssell, J. A. Montgomery Jr., J. E. Peralta, F. Ogliaro, M. J. Bearpark, J. J. Heyd, E. N. Brothers, K. N. Kudin, V. N. Staroverov, T. A. Keith, R. Kobayashi, J. Normand, K. Raghavachari, A. P. Rendell, J. C. Burant, S. S. Iyengar, J. Tomasi, M. Cossi, J. M. Millam, M. Klene, C. Adamo, R. Cammi, J. W. Ochterski, R. L. Martin, K. Morokuma, O. Farkas, J. B. Foresman, D. J. Fox, Gaussian 16 Rev. C.01, (2016).

29. S. Grimme, S. Ehrlich, L. Goerigk, Effect of the damping function in dispersion corrected density functional theory. *Journal of Computational Chemistry* **32**, 1456–1465 (2011).

30. S. Grimme, J. Antony, S. Ehrlich, H. Krieg, A consistent and accurate ab initio parametrization of density functional dispersion correction (DFT-D) for the 94 elements H-Pu. *Journal of Chemical Physics* **132**, 154104–154104 (2010).

31. D. Riepl, A. P. Gamiz-Hernandez, T. Kovalova, S. M. Król, S. L. Mader, D. Sjöstrand, M. Högbom, P. Brzezinski, V. R. I. Kaila, Long-range charge transfer mechanism of the III2IV2 mycobacterial supercomplex. *Nat Commun* **15**, 5276 (2024).

32. A. M. Barragan, A. R. Crofts, K. Schulten, I. A. Solov'yov, Identification of ubiquinol binding motifs at the Qo-site of the cytochrome bc1 complex. *The Journal of Physical Chemistry B* **119**, 433–447 (2014).

33. A. M. Barragan, K. Schulten, I. A. Solov'yov, Mechanism of the primary charge transfer reaction in the cytochrome bc1 complex. *The Journal of Physical Chemistry B* **120**, 11369–11380 (2016).

34. G. M. Arantes, Redox-Activated Proton Transfer through a Redundant Network in the Q_o Site of Cytochrome bc_1. Biophysics [Preprint] (2024). https://doi.org/10.1101/2024.11.22.624873.

35. M. Sarewicz, S. Pintscher, Ł. Bujnowicz, M. Wolska, Artur Osyczka, The High-Spin Heme b L Mutant Exposes Dominant Reaction Leading to the Formation of the Semiquinone Spin-Coupled to the [2Fe-2S]+ Cluster at the Qo Site of Rhodobacter capsulatus Cytochrome bc 1. *Frontiers in Chemistry* **9**, 1–12 (2021).

36. A. Borek, A. Wójcik-Augustyn, P. Kuleta, R. Ekiert, A. Osyczka, Identification of hydrogen bonding network for proton transfer at the quinol oxidation site of Rhodobacter capsulatus cytochrome bc1. *Journal of Biological Chemistry* **299**, 105249 (2023).

37. T. Wenz, P. Hellwig, F. MacMillan, B. Meunier, C. Hunte, Probing the role of E272 in quinol oxidation of mitochondrial complex III. *Biochemistry* **45**, 9042–9052 (2006).

38. A. Osyczka, H. Zhang, C. Mathe, P. R. Rich, C. C. Moser, P. L. Dutton, Role of the PEWY glutamate in hydroquinone-quinone oxidation-reduction catalysis in the Qo site of cytochrome bc1. *Biochemistry* **45**, 10492–10503 (2006).

39. N. Seddiki, B. Meunier, D. Lemesle-Meunier, G. Brasseur, Is Cytochrome *b* Glutamic Acid 272 a Quinol Binding Residue in the bc_1 Complex of *Saccharomyces cerevisiae*? *Biochemistry* **47**, 2357–2368 (2008).

40. B. Wiseman, R. G. Nitharwal, O. Fedotovskaya, J. Schäfer, H. Guo, Q. Kuang, S. Benlekbir, D. Sjöstrand, P. Ädelroth, J. L. Rubinstein, P. Brzezinski, M. Högbom, Structure of a functional obligate complex III2IV2 respiratory supercomplex from Mycobacterium smegmatis. *Nat Struct Mol Biol* **25**, 1128–1136 (2018).

41. J. Zhu, T. Egawa, S.-R. Yeh, L. Yu, C.-A. Yu, Simultaneous reduction of iron-sulfur protein and cytochrome bL during ubiquinol oxidation in cytochrome bc1 complex. *Proceedings of the National Academy of Sciences of the United States of America* **104**, 4864–4869 (2007).

42. P. R. Vennam, N. Fisher, M. D. Krzyaniak, D. M. Kramer, M. K. Bowman, A caged, destabilized, free radical intermediate in the Q-cycle. *ChemBioChem* **14**, 1745–1753 (2013).

43. M. Sarewicz, Ł. Bujnowicz, A. Osyczka, Generation of semiquinone-[2Fe-2S]+ spin-coupled center at the Qo site of cytochrome bc1 in redox-poised, illuminated photosynthetic membranes from Rhodobacter capsulatus. *Biochimica et Biophysica Acta - Bioenergetics* **1859**, 145–153 (2018).

44. Ł. Bujnowicz, M. Sarewicz, A. Borek, P. Kuleta, M. Sarewicz, A. Osyczka, Suppression of superoxide production by a spin-spin coupling between semiquinone and the Rieske cluster in cytochrome bc1. *FEBS Letters* **593**, 3–12 (2019).

45. R. A. Marcus, N. Sutin, Electron transfers in chemistry and biology. *Biochimica et Biophysica Acta* **811**, 265–322 (1985).

46. B. J. Hardy, P. Dubiel, E. L. Bungay, M. Rudin, C. Williams, C. J. Arthur, M. J. Guberman-Pfeffer, A. Sofia Oliveira, P. Curnow, J. L. R. Anderson, Delineating redox cooperativity in water-soluble and membrane multiheme cytochromes through protein design. *Protein Science* **33**, e5113 (2024).

47. G. M. Ullmann, L. Mueller, E. Bombarda, "Theoretical Analysis of Electron Transfer in Proteins: From Simple Proteins to Complex Machineries" in *Cytochrome Complexes-Evolution, Structures, Energy Transduction, and Signaling* (2016), pp. 99–127.

48. S. Bhaduri, V. Stadnytskyi, S. D. Zakharov, S. S. Hasan, Ł. Bujnowicz, M. Sarewicz, S. Savikhin, A. Osyczka, W. A. Cramer, Pathways of transmembrane electron transfer in cytochrome bc complexes: dielectric heterogeneity and interheme coulombic interactions. *Journal of Physical Chemistry B* **121**, 975–983 (2017).

49. S. Lhee, D. R. J. Kolling, S. K. Nair, S. A. Dikanov, A. R. Crofts, Modifications of protein environment of the [2Fe-2S] cluster of the bc1complex: Effects on the biophysical properties of the Rieske iron-sulfur protein and on the kinetics of the complex. *Journal of Biological Chemistry* **285**, 9233–9248 (2010).

50. H. Zhang, S. E. Chobot, A. Osyczka, C. A. Wraight, P. L. Dutton, C. C. Moser, Quinone and non-quinone redox couples in complex III. *Journal of Bioenergetics and Biomembranes* **40**, 493–499 (2008).

Acknowledgments

Funding: This research was funded in whole or in part by National Science Centre, Poland, grant no. 2023/49/B/NZ1/02110 (MS). For the purpose of Open Access, the author has applied a CC-BY public copyright licence to any Author Accepted Manuscript (AAM) version arising from this submission. The research for this publication has been supported by a grant from the Priority Research Area (BioS) under the Strategic Programme Excellence Initiative at Jagiellonian University. We gratefully acknowledge Polish high-performance computing infrastructure PLGrid (HPC Centers: ACK Cyfronet AGH) for providing computer facilities and support within computational grant no. PLG/2023/016712. We also acknowledge infrastructural support by Strategic Programme Excellence Initiative at Jagiellonian University - BioS PRA. We acknowledge the use of AI tools solely for linguistic improvements and text refinement, not for content creation or data analysis.

Authors contributions: Conceptualization: AWA, ŁB, AO, MS. Methodology: AWA, ŁB, MS. Investigation: AWA, ŁB, MS. Visualization: AWA, MS. Funding acquisition: MS. Supervision: MS. Writing – original draft: AWA, MS. Writing – review & editing: AWA, ŁB, AO, MS.

Competing interest: Authors declare that they have no competing interests.